Article

Electronic and Optical Properties of Alkaline Earth Metal Fluoride Crystals with the Inclusion of Many-Body Effects: A Comparative Study on Rutile MgF_2 and Cubic SrF_2

Giancarlo Cappellini [1,*], Jürgen Furthmüller [2], Friedhelm Bechstedt [2] and Silvana Botti [2]

1 Department of Physics, University of Cagliari, CNR-IOM SLACS and ETSF, Cittadella Universitaria di Monserrato, Strada Prov.le Monserrato-Sestu, Km 0.700, Monserrato, 09042 Cagliari, Italy
2 Institute für Festkörpertheorie und -Optik, Friedrich-Schiller-Universität Jena, and ETSF, Max-Wien-Platz 1, D-07743 Jena, Germany
* Correspondence: giancarlo.cappellini@dsf.unica.it

Abstract: We conducted a systematic investigation using state-of-the-art techniques on the electronic and optical properties of two crystals of alkaline earth metal fluorides, namely rutile MgF_2 and cubic SrF_2. For these two crystals of different symmetry, we present density functional theory (DFT), many-body perturbation theory (MBPT), and Bethe–Salpeter equation (BSE) calculations. We calculated a variety of properties, namely ground-state energies, band-energy gaps, and optical absorption spectra with the inclusion of excitonic effects. The quantities were obtained with a high degree of convergence regarding all bulk electronic and optical properties. Bulk rutile MgF_2 has distinguished ground-state and excited-state properties with respect to the other cubic fluoride SrF_2 and the other members of the alkaline earth metal fluoride family. The nature of the fundamental gaps and estimates of the self-energy and excitonic effects for the two compounds are presented and discussed in detail. Our results are in good accordance with the measurements and other theoretical–computational data. A comparison is made between the excitation and optical properties of bulk rutile MgF_2, cubic SrF_2, and the corresponding clusters, for which calculations have recently been published, confirming strong excitonic effects in finite-sized systems.

Keywords: fluoride compounds; electronic and optical properties; quasiparticle and excitonic effects; DFT theory; crystal symmetry; UV crystal materials

1. Introduction

Fluorides and fluorite-type crystals have received much interest for their intrinsic optical properties and their potential applications in optoelectronic devices, in particular for those operating in the ultraviolet (UV) region of the electromagnetic spectrum. CaF_2, e.g., shows a direct band gap at the Γ point of the first Brillouin zone (1st BZ) of 12.1 eV and an indirect gap of 11.8 eV [1]. It is a highly ionic system with the cubic (c) fluorite crystal structure with three atoms per unit cell and space group $Fm\bar{3}m$ [2]. In the present work, we investigate the compounds rutile MgF_2 (r-MgF_2) and cubic SrF_2 (c-SrF_2), with light and heavy cations belonging to the group IIA, to determine their electronic and optical properties using different theoretical and computational schemes. The calculations are based on state-of-the-art many-body schemes, e.g., perturbative GW (i.e., G_0W_0), self-consistent, and full GW, the solution of the Bethe–Salpeter equation (BSE), etc., which account for the quasiparticle (QP) band structure and the mutual interaction between excited electrons and holes, [3], and should start from well-converged ground-state calculations in the framework of DFT [4,5].

To consider the strategic roles played by the fluorites in modern applied research, we look at the deep ultra-violet (DUV) technology used for photolithography and the EUV (extreme UV) technique [4]. Such technologies make the study of the electronic and optical

properties of the alkaline earth metal fluorides important, which show transparency in UV energy windows used to build lenses, mirrors, prisms, masks, and cladding surfaces. A better understanding of their optical properties can lead to the development of these materials and allow theoretical and experimental investigations focusing on electronic and optical properties of surfaces, including related problems, e.g., photomolecular contaminations, or the presence and the role of defects in the bulk or at the surfaces. These points have not been completely explored in the literature and will be part of a future research campaign [5–8].

Experimental studies on difluorides have been performed for several years. To study optical, structural, and electronic properties of alkaline earth metal fluorides systems, different experimental techniques have been used, such as optical reflectance [1], discharge tube experiments, [9] dielectric loss techniques [10], photoelectron spectrometry measurements [11], light absorption and spectrophotometry techniques [12,13], neutron diffraction [14], and polarized light schemes [15,16].

Another relevant research issue to be considered is the use of ultraviolet radiation (UV) for biological, pharmacological, and medical applications, e.g., the radiation disinfection schemes in relation to the outbreaks caused by SARS-CoV-1 and SARS-CoV-2 viruses [17]. For this kind of radiation, the use of specific tools and instruments, e.g., mirrors, cuvettes, test tubes, bulbs, container tubes, separation, and cladding surfaces made by materials specific for the UV is requested in relation to the radiation disinfection-antimicrobial/antiviral issues [18–22]. As a consequence, there has been a boost in the research on transparent materials that could be produced, controlled, and used in specific UV radiation disinfection devices. The present study contributes to that research field, completing the scenario on the electronic and optical properties of bulk alkaline earth metal fluorides treated within state-of-the-art theoretical–computational methods.

Some bulk cubic fluorides were considered by participants of the present collaboration. They studied the cubic fluorides by means of DFT with the local density approximation (LDA) for the exchange–correlation energy [23]. The ground-state electronic properties of the bulk cubic structures of CaF_2, SrF_2, BaF_2, CdF_2, HgF_2, and β-PbF_2 were studied with the use of a plane wave expansion of the wave functions. General trends of the structural parameters were considered together with electronic energy bands and transition energies. The same authors later faced the calculations of the electronic and optical properties of two of the above-mentioned bulk compounds, namely CdF_2 and BaF_2, using state-of-the-art computational techniques for the quasiparticle band structures and excitonic effects [24,25]. The results agreed well with existing experimental data, in particular the absorption spectra in a wide energy range. The scope of the present paper involves extending those methods to r-MgF_2 and c-SrF_2, i.e., to study their electronic excitations and optical properties. This study evaluated the validities of approximate methodological treatments. Fluoride compounds were recently tackled to test efficient quasiparticle–calculation schemes for solid crystalline solids, e.g., the $DFT - 1/2$ and the pseudo-self-interaction-corrected DFT method (PSIC) [26–28].

On the experimental side, for cubic SrF_2, there have been experimental studies performed for decades, i.e., electron energy loss measurements, [29] dielectric measurements as functions of temperature and pressure [10], and UPS and XPS spectral analyses [11,30]. On the other hand, there have been few theoretical and computational contributions to the study of the electronic properties of cubic SrF_2 based on different techniques [31,32]. c-SrF_2 shows important features in the V-UV (vacuum-UV) region. Therefore, studies have been performed for decades on its pure form [29] and doped forms regarding the V-UV energy range [33]. Recent applications of c-SrF_2-based phosphors operating in the V-UV should also be considered [34]. Regarding the c-SrF_2 crystal, which shows intermediate electronic and optical properties in the group of cubic alkaline earth metal fluorides, the need for theoretical and computational results after state-of-the-art schemes is timely.

MgF_2, whose cation retains in the group-IIA of the alkaline earth metals, the first position, with respect to the metal atomic radii, is an anisotropic wide-band-gap crystalline

system. It crystallizes in the rutile (r) structure, with tetragonal $P4_2/mnm$ symmetry, and it is a relevant optical material. It is transparent in a very wide range of photon energies. One of its main applications is in the vacuum ultraviolet spectroscopy (VUS), where it is used as a deposited slab placed on aluminum mirrors and gratings. This is to protect aluminum itself from oxidation, maintaining UV transparency. For rutile MgF_2, experimental studies have existed for several years, e.g., electron energy loss studies [11] and a few computational studies [35]. Recently, ground-state properties of the $MgF_2(011)$ and $MgF_2(111)$ surfaces were calculated [36,37]. For bulk r-MgF_2, advanced techniques were used to calculate the one- and two-particle effects in the electronic and optical properties [37]. However, for bulk r-MgF_2, the present study clarifies different fundamental points, i.e., the scheme to calculate the dielectric screening function and essential approximation used to tackle the excitonic effects and address issues not covered by previous studies. For r-MgF_2 observables as first peak energy positions, exciton binding energy and dielectric constant for the two principal directions of the crystal are reported here for the first time. Moreover, a detailed analysis of how different self-consistency procedures affect the results of self-energy schemes applied to the two materials under study is presented.

Interest in the electronic and optical properties of alkaline earth metal fluoride clusters is an important motivation for the present studies [38–42]. In Reference [38] the authors focused their attention on $(MF_2)_n$ nanoparticles with $n = 1, 2, 3$ and M = Mg,Ca,Sr,Ba. For the three stable smallest cluster classes, two main facts clearly appeared: a consistent redshift of the onset energy and a corresponding boost of the exciton binding energy. The presence or absence of these strong effects are the selective criteria for optical experiments, to check the creation and existence of such finite-size portions in the target. The present work on bulk r-MgF_2 and c-SrF_2 allows for a systematic comparison of structural, electronic, and optical properties, calculated within most modern techniques.

2. Computational Methods and Resulting Ground-State Properties

We present structural data and cohesive properties of the two metal difluorides; technical parameters will be proposed and discussed here. All calculations for the ground state, the excited state, and the optical properties were performed with the VASP simulation package [43,44]. All ground-state fits were done employing the Vinet equation of state and the cohesive energy E_0 is given with respect to the sum of energies of free spin-polarized atoms [45]. The values were obtained using the PBEsol exchange–correlation (XC) functional [46]. It delivers the best comparison to the experimental data [24]. We also present the following tests for each fluoride using different XC functionals.

MgF_2 crystallizes in the simple tetragonal rutile structure with six atoms per unit cell. Rutile itself is an oxide mineral made of titanium dioxide (TiO^2), which is the most common natural form of TiO^2 with peculiar features as the highest refractive indices in the visible, large birefringence and dispersion. The unit cell of this crystal is characterized by two lattice constants, *a* and *c*. The simple tetragonal Bravais lattice has the primitive vectors (*a*,0,0) and (0,*a*,0) and (0,0,*c*). An additional structural parameter for r-MgF_2, as an internal degree of freedom, is the Wyckoff parameter x [47]. The six atomic positions are then given as (0,0,0) and (1/2,1/2,1/2) for Mg and (x,x,0), (−x,−x,0), (1/2+x,1/2−x,1/2) and (1/2−x,1/2+x,1/2) for F with x = 0.303326, given in units of lattice vectors.

The SrF_2 crystal belongs to the space group $Fm\bar{3}m$ and possesses a face-centered cubic fluorite structure. CaF_2, SrF_2, and BaF_2 all possess the face-centered cubic fluorite structure with three atoms per unit cell, with the cation at position (0,0,0) and the two fluorine anions at (lattice) coordinates ±(1/4,1/4,1/4). For them, the only relevant structural parameter is the cubic lattice constant *a*. In Table 1, the ground-state properties from the present calculations for both crystals are listed.

Table 1. Ground-state properties of the difluoride crystals r-MgF$_2$ and c-SrF$_2$. The lattice parameter a of both structures and parameter c for the rutile are reported together with the bulk modulus and its pressure derivative.

PBEsol	r-MgF$_2$	c-SrF$_2$
a [Å]	4.6313	5.7744
c [Å]	3.0558	—
c/a	0.6598	—
B$_0$ [MPa]	97.1	72.8
dB$_0$/dp	4.69	4.71

All calculations were performed for the structure obtained with the PBEsol exchange–correlation functional, ref. [46] with plane-wave cutoffs and k-samplings listed in Table 2, thereby E_{cut} is the "soft" cutoff for the non-norm-conserving (partial) wave function and E_{aug} is the plane-wave cutoff for the plane-wave-expanded "intermediate" PAW augmentation charges.

Table 2. Cutoff parameters and ground-state energy of the difluoride crystals under study. The total energy for the simulation cell E_0, the cutoff energy E_{cut} for non-norm-conserving (partial) wave functions, and the cutoff energy E_{aug} for the plane-wave expanded "intermediate" PAW augmentation charges are given. On the last line, the k-point mesh used for the BZ integration is listed.

PBEsol	r-MgF$_2$	c-SrF$_2$
E$_{cut}$ [eV]	1020	640
E$_{aug}$ [eV]	1700	1640
E$_0$ [eV]	-30.1122	-16.3389
k-point set	$12 \times 12 \times 18$	$12 \times 12 \times 12$

Concerning the PAW data set, we used for F a rather hard and accurate potential, with a $4f$-component as the local potential and non-local $s-$, $p-$, and $d-$projectors. The Mg-potential is a slightly revised version of the Mg "sv" potential supplied with VASP, while for Sr the standard "sv" potential was used. The potentials for Mg and Sr include s and p core states and corresponding (occupied) s and (unoccupied) p valence states (one principal quantum number higher), as well as (unoccupied) $3d$ states for Mg, and (occupied) $3d$ and (unoccupied) $4d$ states for Sr. Local potentials are, in these cases, "cutted", as well as all-electron potentials, except for Mg, where a $4f$ potential was used as the local potential (together with a "stabilizing" $5f$-like extra non-local f-projector to enhance f-potential transferability).

We calculated the ground-state properties considering different XC potentials. These data are of fundamental importance for the treatment of electronic excitations and optical properties, as we will discuss in the following paragraphs. The different XC functionals considered are as follows: standard-PBE, [48] AM05, [49], and LDA (Ceperley–Alder) [50]. Technical parameters (energy cutoffs, k-samplings) were the same as before. Results for each individual material are reported in Table 3. For comparison, in the case of r-MgF$_2$, the experimental values are from Reference [51], while for c-SrF$_2$, experimental values were obtained from References [52,53].

Overall, from Table 3, one can state that PBEsol gives the closest results to the experiment. For example, the lattice parameter a in the case of r-MgF$_2$, calculated with PBEsol, shows a deviation in the order of 0.1%, while in the case of c-SrF$_2$, the deviation from the experiment for the same observable is of the order of 0.4%. The AM05 results are approximately of the same quality. For the PBE XC scheme (with the typical under-binding effect due to gradient corrections), the results show more significant deviations from the experiment; for LDA calculations (strong over-binding due to the local approximation), the comparison with experiment is worse. For these reasons, structures obtained with PBEsol were used for the present study for the calculation of energy bands and optical properties.

Table 3. Ground-state properties of r-MgF$_2$ and c-SrF$_2$. For r-MgF$_2$ in the upper part of the table, the lattice parameters a, c, their ratio c/a, and the x parameter are reported as functions of the XC potential used for the calculations in the first four rows. In the following three rows, the bulk modulus, its pressure derivative, and the total energy of the unit cell are given. In the last column, the experimental values from Reference [51] are listed. In the lower part of the table, we report the ground-state properties of c-SrF$_2$. The lattice parameter a was reported as in the first row, i.e., as a function of the different XC potentials used. In the following three rows, we provide the bulk modulus, its pressure derivative, and the total energy of the unit cell. In the last column, the experimental data after Reference [52] and Reference [53] are given.

r-MgF$_2$	PBEsol	PBE	AM05	LDA	EXP
a[Å]	4.6313	4.6928	4.6649	4.5638	4.6249
c[Å]	3.0558	3.0875	3.0741	3.0194	3.0520
c/a	0.6598	0.6579	0.6590	0.6616	0.6599
x	0.3033	0.3035	0.3037	0.3030	0.3027
B_0[GPa]	97.1	90.1	91.6	111.2	101 ± 3
dB_0/dP	4.69	4.74	4.73	4.64	4.2 ± 1.1
E_0[eV]	-30.1122	-28.7552	-29.7466	-33.0805	
c-SrF$_2$	**PBEsol**	**PBE**	**AM05**	**LDA**	**EXP**
a[Å]	5.7744	5.8712	5.8094	5.6813	5.7994
B_0[GPa]	72.8	64.5	67.5	84.9	$67.1 - 74.6$
dB_0/dp	4.71	4.73	4.74	4.61	4.2 ± 1.1
E_0[eV]	-16.3389	-15.6630	-16.0187	-17.8951	

3. Electronic Excitations in r-MgF$_2$ and c-SrF$_2$

Many-body effects on the electronic and optical spectra of the difluoride compounds are calculated using DFT and several many-body perturbation schemes on top. The GW approximation for the exchange–correlation self-energy is used to describe the single-particle excitations, particularly to calculate the QP electronic energy bands and densities of states of these fluorites. The two-particle effects in optical spectra are included by solving the Bethe—Salpeter equation (BSE) for the two-particle Green function with screened electron–hole attraction and repulsive electron–hole exchange. The optical absorption spectra are compared with existing and previous experimental and theoretical results. The reasons for the agreements or discrepancies are then fully discussed.

The exchange–correlation self-energy Σ in the Hedin scheme [54–58] has the form of the product of a dynamically screened Coulomb interaction W and the single-particle Green function G in real-time space. Using the RPA approximation for W, kept fixed during the iteration of Hedin's equations (with $W = W_0$), and DFT wave functions in the single-particle Green function G_0, the self-energy has the form $\Sigma = \Sigma_0 = G_0 W_0$, which is known as the $G_0 W_0$ method. This scheme usually gives excellent results for the GW eigenvalues of solids (band gaps, bandwidths, and band dispersions) [55,56]. An improved GW treatment of the QP band structure is the so-called generalized KS (gKS) method [59,60]. Nonlocal exchange–correlation potentials with the inclusion of partial or screened exact exchanges in the gKS approximation are applied in the KS equations. These gKS methods are usually efficient, but approximate, GW schemes [61]. A gKS starting point (leaving a gap error of 3.0 eV for r-MgF$_2$ and of 2.4 eV for c-SrF$_2$) can be considered a good starting point for both compounds.

The iteration starts from the gKS equations, with self-energy chosen as the nonlocal HSE06 hybrid potential [62,63]. In the second step, the GW corrections are determined with the perturbative $G_0 W_0$ scheme. The frequency dependence of the RPA dielectric function in the screened Coulomb interaction (W_0) is taken into account. Neither plasmon pole models [64] nor model dielectric functions [56,65] were used. Several steps arise. The band structure and DOS were first determined within the PBEsol scheme, then the HSE06 method was utilized, and finally, we used the $G_0 W_0$ scheme on top of HSE06.

In this zeroth iteration, the QP gaps are larger by about 0.4 eV for r-MgF$_2$ and by 0.2 eV for c-SrF$_2$ than the experimental ones. For these materials, the single-shot GW (G$_0$W$_0$) method does not give a definitive result for the true QP energies. For this reason, self-consistent quasiparticle energy calculations within the GW scheme were also performed. We employed the GW$_0$ scheme iterating the Green function only, as well as the scQP-GW scheme (also known as the evGW scheme), updating the eigenvalues in both G and W, but maintaining the HSE wave functions in all iteration steps. It was demonstrated that the iterative GW schemes give gap values in better agreement with respect to the experimental values, particularly for the parent compound CdF$_2$ [25,66,67].

For HSE06 used as the GW starting point in the GW and BSE schemes, the same cutoffs that were used for the ground-state calculations were kept, but k-samplings had to be reduced (an $8 \times 8 \times 8$ mesh for the c-SrF$_2$ and an $8 \times 8 \times 12$ mesh for r-MgF$_2$).

3.1. Energy Gaps for r-MgF$_2$ and c-SrF$_2$

The r-MgF$_2$ crystal possesses a direct gap at Γ, where the valence band maximum, mainly composed of degenerate F $2p$ states, exhibits a crystal-field splitting of. The bottom of the conduction band is composed of Mg $3s$ states and hence no crystal-field splitting can occur for the lowest conduction band. We find a non-degenerate highest valence band state with a p_z-character accompanied by a p_x-/p_y based double degenerate second valence band, split off by an amount of Δ_{cf} below the top p_z band. This splitting is also visible later in the optical spectra since, according to the selection rules, p_z-s transitions are only allowed for light polarization perpendicular to the z-axis (being identical to the tetragonal c-axis) while p_x/p_y-s transitions are only allowed for light polarization parallel to the z (or c)-axis. Hence, the absorption onsets for different light polarizations are split as well. The direct QP gap and the crystal-field splitting Δ_{cf} obtained with different approximations are listed below in Table 4.

In contrast to r-MgF$_2$, for c-SrF$_2$, we find an indirect fundamental gap as for the other cubic-earth-alkaline fluorides, i.e., c-CaF$_2$ and c-BaF$_2$ [23,23]. The bottom of the conduction band is also found at Γ and composed of Sr $5s$ states, while the top of the valence bands is composed of F $2p$ states that are triple-degenerate at Γ, without spin-orbit (SO) coupling (and hence we obtain small SO splittings for the F $2p$ bands). The maximum of the valence band is located at the X point and is found approximately 0.1 eV above the valence band at Γ. The QP values for the direct gap at Γ and the indirect fundamental gap $X - \Gamma$ obtained with different approximations are reported in Table 4.

Table 4. Quasi-particle energies for the fundamental energy gaps of r-MgF$_2$ and c-SrF$_2$ calculated with different approximations are reported and compared with available experimental results (for r-MgF$_2$ from Reference [37] and for c-SrF$_2$ from Reference [1]). B3PW refers to hybrid exchange–correlation potential calculations: the value for r-MgF$_2$ from Reference [68], the values for c-SrF$_2$ after References [69,70]. The row "Other" refers to the theoretical data for r-MgF$_2$ from Reference [37] and for c-SrF$_2$ from References [32,71] in parentheses.

r-MgF$_2$	Direct Gap [eV]	Δ_{cf} [eV]
PBEsol	6.921	-0.320
HSE06	9.433	-0.289
G$_0$W$_0$	12.800	-0.291
GW$_0$	13.243	-0.285
scQP-GW	13.945	-0.277
B3PW	9.48	-
Other	12.17	-
Exp.	12.4	-0.2

Table 4. *Cont.*

c-SrF$_2$	Direct Gap [eV]	Indirect Gap [eV]
PBEsol	6.932	6.827
HSE06	9.172	9.072
G$_0$W$_0$	11.437	11.316
GW$_0$	11.820	11.700
scQP-GW	12.490	12.375
B3PW	11.306/10.96	-
Other	11.24	11.20(7.55)
Exp.	11.25	—

The G$_0$W$_0$ results appear to be the closest to the experimental values (see also the discussion on the effects of the use of different XC potentials in References [24,25]). However, experimental gap values are always determined indirectly from excitonic spectra, attempting to find some independent particles, such as features that can be extrapolated to zero absorption. The only safe and experimental values are the excitonic gaps (onset energies of absorption in the optical spectra), which are located at 11.6 eV in the case of MgF$_2$ and 10.6 eV in the case of c-SrF$_2$ [72,73].

In the following section, where we present optical absorption spectra, and compare experimental and theoretical excitonic gaps, in the case of MgF$_2$, we find that GW$_0$ results are closer to the experiment than G$_0$W$_0$ results. For the case of c-SrF$_2$, we find that GW$_0$ and scQP-GW results are approximately equally close to the experiment, while GW$_0$ results are still marginally closer to the experiment (experimental values are found almost halfway in between these two theoretical results). This follows an interesting chemical trend. In our previous papers on c-BaF$_2$ [24] and CdF$_2$ [25], we found that only scQP-GW gave results close to the experiment [74]. Now, for c-SrF$_2$, we find that the experimental results are almost halfway between GW$_0$ and scQP-GW. For the sake of comparison, an additional calculation was performed for c-CaF$_2$ within the same schemes and accuracies used in the r-MgF$_2$/c-SrF$_2$ cases. For CaF$_2$, we find that GW$_0$ results for the direct fundamental gap (12.3 eV) are closer to the experiment (12.1 eV from Reference [1]). For r-MgF$_2$, GW$_0$ results are the closest to the experiment (where experimental results are somewhat below theoretical results) although G$_0$W$_0$ results are only slightly further from the experiment. So, it leaves the impression that going down from Mg to Ba, we have to increase the degree of self-consistency in our GW calculations, at least starting with HSE06 electronic structures. This fact is related to the so-called under-screening problem recently addressed in the literature [75–77].

Starting from DFT-PBEsol band structures with 2.1–2.5 eV, smaller gaps tend to underestimate the gaps of difluorides. However, adding scQP-GW corrections obtained with the HSE06 starting points of about 3.5 eV (r-MgF$_2$) of 3.3 eV (c-SrF$_2$) (see Table 4) would open up the PBEsol gaps.

With respect to the band gap problem, we should also remember the existence of other methods used to tackle that issue, e.g., those based on hybrid exchange–correlation functionals. For example, the band gaps of related ABO3 perovskites, calculated recently by means of the hybrid exchange–correlation functionals B3PW or B3LYP, are found to show good comparison with the experiments [78].

One should consider that both materials studied here are highly polar; therefore, one can expect that the self-consistent GW energy gaps overestimate the experimental data due to the lack of renormalization effects related to lattice polarization [79]. Including phonon contributions to the screening would lead to the closure of the gap (due to longitudinal optical phonons), particularly in (highly) polar compounds [79–81]. However, the treatment of lattice polarization effects is out of the scope of the present calculations on bulk r-MgF$_2$ and c-SrF$_2$ electronic properties. We will tackle this point in future work.

3.2. Quasiparticle Energy Bands for r-MgF$_2$ and c-SrF$_2$

We discuss the QP electronic energy bands of r-MgF$_2$ and c-SrF$_2$ in the approximation schemes discussed above. The principal results of the calculations described in the present paragraph are reported in Figure 1 (Energy bands GW$_0$ and G$_0$W$_0$ for r-MgF$_2$) and Figure 2 (GW$_0$ and scQP-GW for c-SrF$_2$). The analysis of the two figures shows that for both materials the different GW approaches used to calculate the QP energies give rise to similar bands. For r-MgF$_2$ (the reported bands were obtained within the GW$_0$ and G$_0$W$_0$ schemes) the lowest conduction bands lie about 13 eV above the valence band maximum (VBM), while the shallow F 2p valence bands are found in the range 0 to -5 eV and the deep F 2s valence bands in the range -22 to -23 eV. The band positions and dispersions obtained within the two GW methods are very similar for r-MgF$_2$. The main effect of adding self-consistency in G is just some small scissor-like extra gap opening, more precisely an almost rigid upward shift of the conduction bands of about 0.4 eV.
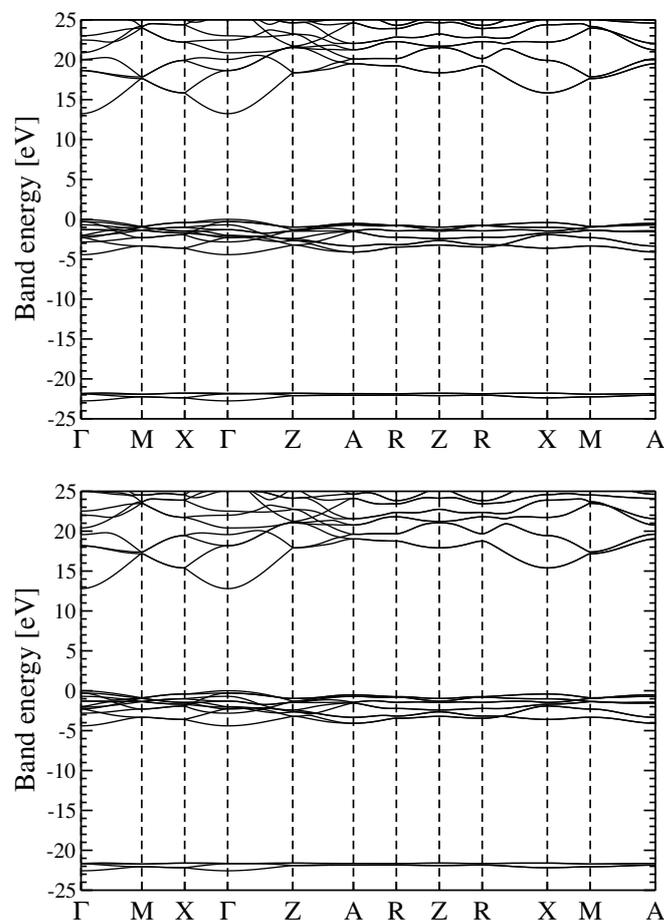

Figure 1. QP energy bands for r-MgF$_2$ in the GW$_0$ scheme (**top**) and within the G$_0$W$_0$ method (**bottom**). See text for details.

On the other hand, for c-SrF$_2$ (the reported bands were obtained within the GW$_0$ and the scQP-GW schemes), the conduction bands are found above 12 eV, the shallow F 2p valence bands are found in the range of 0 to -4 eV, additional shallow Sr 4p valence bands are in the range -12 to -13 eV, and the deep F 2s valence bands are in the range -21 to -22 eV in both schemes. Moreover, for c-SrF$_2$, the two methods outlined here give very comparable results for the dispersion of bands and scQP-GW adds the approximate extra 0.7 eV scissor shift to the conduction bands over GW$_0$.

For the energy bands, it seems that the different theoretical schemes used here produce similar band dispersion paths and variations in the gaps of the order of some hundreds of

meV; we will see in the following paragraph that optical absorption spectra may depend (in a more critical way) on the computational scheme used to calculate the QP energies.
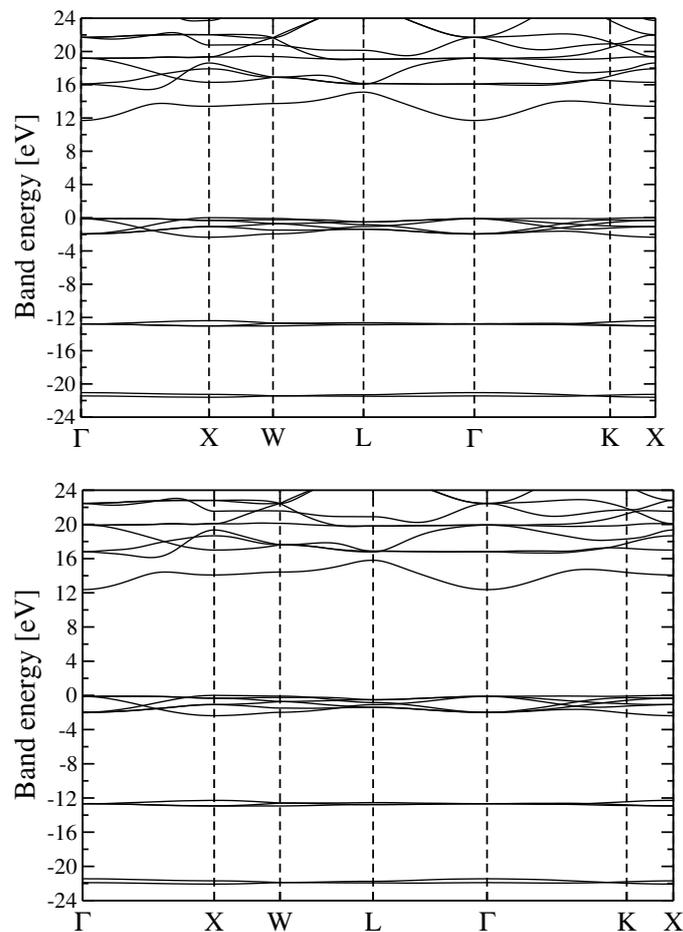

Figure 2. QP energy bands for c-SrF$_2$ in the GW$_0$ scheme (**top**) and the scQP-GW (**bottom**) scheme. See text for details.

4. Dielectric Function and Optical Absorption Spectrum of MgF$_2$ and SrF$_2$

Excitonic effects play a fundamental role in the correct determination of the optical absorption coefficient and dielectric functions of the materials under study. Excitons may represent two limiting cases. In small dielectric constant materials, the Coulomb attraction between an electron and a hole is strong, and the excitons tend to have a small spatial extent of the same order as the bond lengths. In this case, one speaks about Frenkel excitons, which show binding energy ranging from 0.1 to more than 1 eV. The exciton radius for such a system is a few Å only [24,25,82]. On the other hand, in semiconductors, the dielectric constant is generally quite large. As a consequence, the dielectric screening reduces significantly the Coulomb attraction between electrons and holes, and the corresponding exciton binding energies are much smaller than the band gaps. In this limit, the so-called Wannier—Mott (WM) excitons appear. In the WM case, the strength of the binding is typically of the order of 10 meV [83,84].

The study of the excitons and the resulting optical spectra requires the diagonalization of the proper electron–hole Hamiltonian in a Bloch basis to solve the BSE equations [3,57,85]. As the rank of the electron–hole Hamiltonian matrix (determined by the number of k-points and conduction-valence band pairs) is extremely relevant, its direct diagonalization is often hard due to large CPU and memory requirements. Therefore, we apply a numerically more efficient scheme [25,66]. This method is founded in the time evolution of the exciton state. It directly delivers optical spectra, but no exciton eigenvalues and eigenfunctions are explicitly produced [25,66]. This method generates optical spectra with very good

agreement compared to the experimental data and is identical to spectra outputs obtained by the matrix diagonalization scheme.

As it is based on a matrix–vector multiplication, it implies an $O(N^2)$ dependence on the number of operations and therefore allows efficient allocation of the multiplications on several processors of a parallel calculator [66,86]. For the GW and BSE calculations, a Γ-centered $8 \times 8 \times 12$ ($8 \times 8 \times 8$) is used for r-MgF_2 (c-SrF_2). A minimum of fifty unoccupied bands have to be considered in the calculations to tackle the electron–hole pair interaction precisely.

The chosen maximum transition energy cutoff of 60 eV (90 eV) for r-MgF_2 (c-SrF_2) corresponds to about 59 (83) unoccupied bands for r-MgF_2 (c-SrF_2). Together with 16 (10) valence bands, the resulting approximate rank of the excitonic Hamiltonian matrix is 580000 (22700) for r-MgF_2 (c-SrF_2). For the representation of the frequency-dependent dielectric function $\varepsilon(\omega)$, screened exchange integrals, and four-orbit at integrals in the GW and BSE schemes, a plane-wave cutoff is used of 510 eV (475 eV) for r-MgF_2 (c-SrF_2).

In Figure 3, dielectric function components for r-MgF_2 and c-SrF_2 in the GW_0 scheme are shown. In Figure 4, the imaginary part of the dielectric function in $\varepsilon(\omega)$ was reported using the method by Schmidt et al. [25,66]. In that figure, the BSE dielectric function components for r-MgF_2 in the BSE scheme (for the two components of the polarization) and c-SrF_2 were computed on top of the G_0W_0 and scQP-GW, respectively, self-energy calculations. The real parts were derived by a Kramers—Kronig (KK) transformation.

The comparison with the experiments is particularly interesting and important for both materials. The possibility to choose the degree of self-consistency between different QP schemes allow for a very satisfactory comparison between theory and experiment. From Figures 5 and 6, for the imaginary and real parts of the dielectric function of r-MgF_2, we can find a one-to-one correspondence between the peaks and structures in theory and experiments. Nevertheless, the imaginary parts calculated within the GW_0 scheme for both crystals show a very good comparison between theory and experiment for the very first peak, which represents a bound exciton with excitation energy below the direct QP gap. The difference defines the exciton binding energy $E_{Bind} = 1.0 - 1.1$ eV for r-MgF_2 depending on light polarization or $E_{Bind} = 1.4$ eV for c-SrF_2. In the real part of the dielectric functions, on the other hand, the sequence of the first maximum–minimum–second maximum also coincides with the theory and experiment. An overestimation of the experimental data takes place around 23 eV for r-MgF_2 and around 32 eV for c-SrF_2, but these reduced mismatches do not invalidate the overall theory–experiment agreement for this observable.

In Table 5, the energies of the relevant optical absorption features were reported for the fluorides r-MgF_2 and c-SrF_2. The first peak energy position at the absorption onset, the excitation energy of the lowest exciton, and the dielectric constant ε_∞ values are reported using different BSE and GW schemes. These quantities are compared with the corresponding experimental values (fourth column). In the case of r-MgF_2 both the values for the two principal directions of the crystal are given. The effect of the anisotropy on the computed values gives rise to extremely small differences of the order of 3% for the peak position E_{Peak}, less than 10% in exciton binding energy E_{Bind}, and less than 2% in the dielectric constant ε_∞. For r-MgF_2, the best agreement with experimental data is found with the results from the BSE+GW_0 scheme which reproduces the experimental value for E_{Peak} within 2%. Even if the BSE(scQP-GW) value is closer to the experiment for ε_∞, its deviation from the BSE(GW_0) result is less than 1%. On the other hand for c-SrF_2 it seems that both schemes BSE(scQP-GW) and BSE(GW_0) reproduce the experimental data with almost the same accuracy with a calculated value of E_{Peak} within 2% from the measured one (+2% for BSE(scQP-GW), -2% for BSE(GW_0)). There is a clear tendency for overestimation of the exciton binding energies and dielectric constants in all many-body approaches studied. This fact is related to the use of ε_∞ without including the phonon contributions in the screening. The discrepancies are much smaller for the position of the first excitonic absorption peak. Indeed, the theoretical (in BSE-GW_0 quality) and experimental energies only deviate by 0.1–0.2 eV, i.e., by 1–2%.

Table 5. Relevant optical absorption observables and dielectric constants of the difluorides r-MgF$_2$ and c-SrF$_2$. The first peak energy position at the onset, the binding energy of the exciton and the ε_∞ values are reported as obtained in different BSE and GW schemes as discussed in the text and compared with corresponding experimental values from Reference [37] and Reference [29] (fourth column). In the case of r-MgF$_2$, both the values for the two principal directions of the crystal were reported.

r-MgF$_2$	BSE (G$_0$W$_0$)	BSE (GW$_0$)	BSE (scQP-GW)	EXP
E$_{Peak,\|\|}$[eV]	11.37	11.81	12.23	11.6
E$_{Peak,\perp}$[eV]	11.76	12.21	12.62	12.1
E$_{Bind,\|\|}$[eV]	1.14	1.14	1.43	0.8
E$_{Bind,\perp}$[eV]	1.04	1.03	1.32	0.5
$\varepsilon_{\infty,\|\|}$	1.88	1.85	1.84	1.67
$\varepsilon_{\infty,\perp}$	1.91	1.890	1.87	1.68
c-SrF$_2$	**BSE (G$_0$W$_0$)**	**BSE (GW$_0$)**	**BSE (scQP-GW)**	**EXP**
E$_{Peak}$[eV]	10.01	10.40	10.83	10.6
E$_{Bind}$[eV]	1.43	1.42	1.66	0.65
ε_∞	2.18	2.15	2.13	2.08
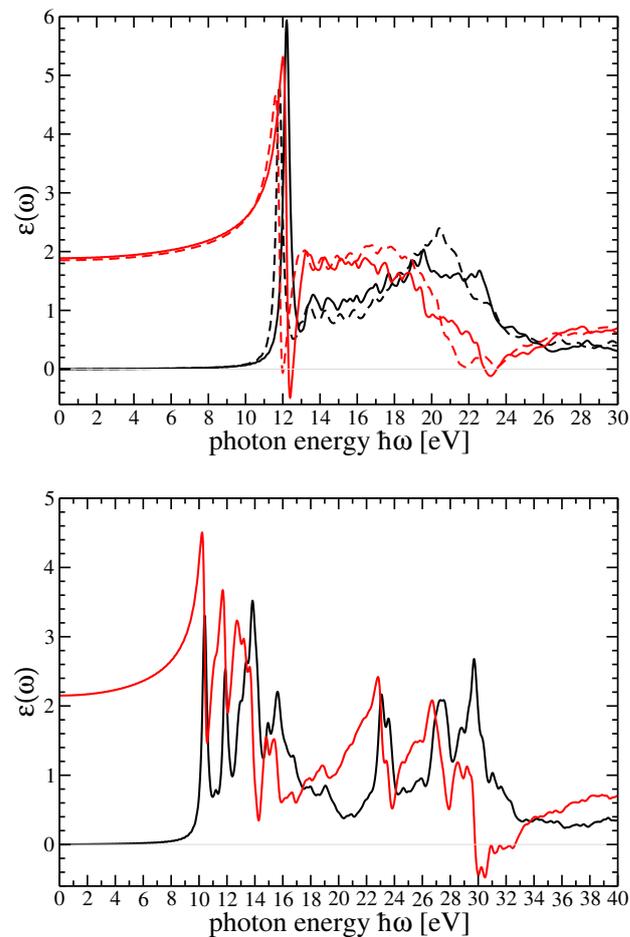
Figure 3. Dielectric function components for r-MgF$_2$ (**top**) and c-SrF$_2$ (**bottom**) in the BSE scheme on top of GW$_0$ bands (see text). Red lines refer to the real part and black lines to the imaginary parts of the dielectric functions. In the case of c-MgF$_2$, full lines refer to the *zz* component and broken lines to the *xx* and *yy* components.
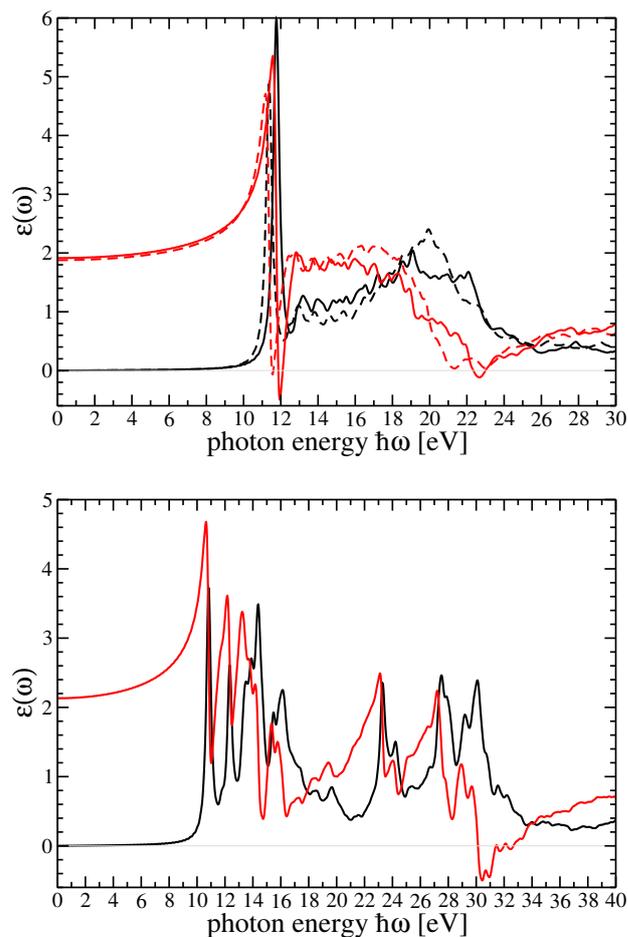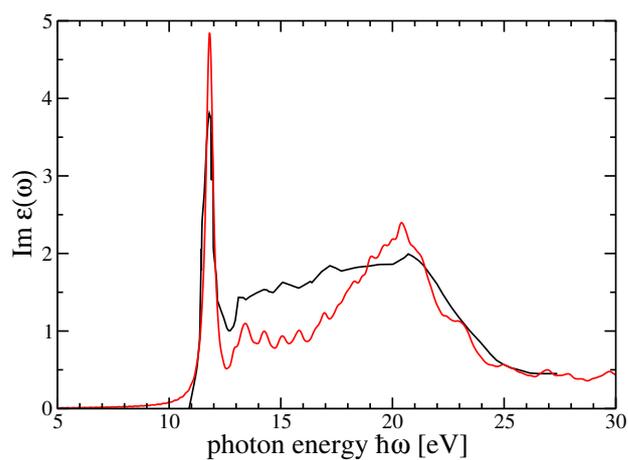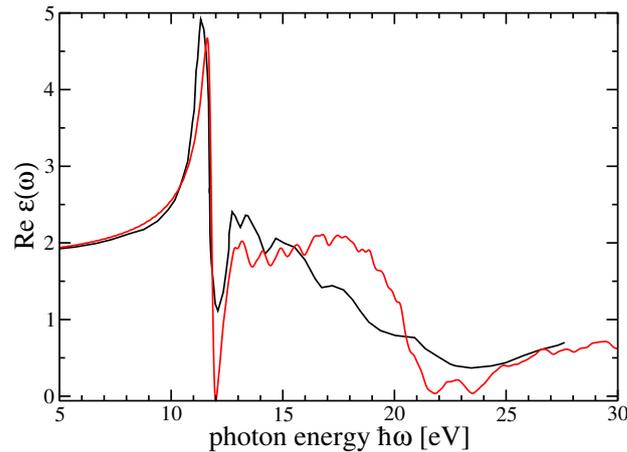
Figure 4. Dielectric functions of r-MgF$_2$ (**top**) resulting in the BSE scheme (for the two components of light polarization) and of c-SrF$_2$ (**bottom**) on top of G$_0$W$_0$ and scQP-GW respectively self-energy calculations (see text). Red lines refer to the real part and black lines to the imaginary parts of the dielectric functions. In the case of r-MgF$_2$, full lines refer to the *zz* component and broken lines to the *xx* and *yy* components.

Figure 5. *Cont*.

Figure 5. Dielectric functions components (**top**: imaginary part, **bottom**: real part) of r-MgF_2 in the BSE scheme on top of GW_0 energies in comparison with the experiment reported in Reference [37] (see text). Red lines refer to our calculated spectra and black lines to the experimental data. Isotropic averages only are displayed.
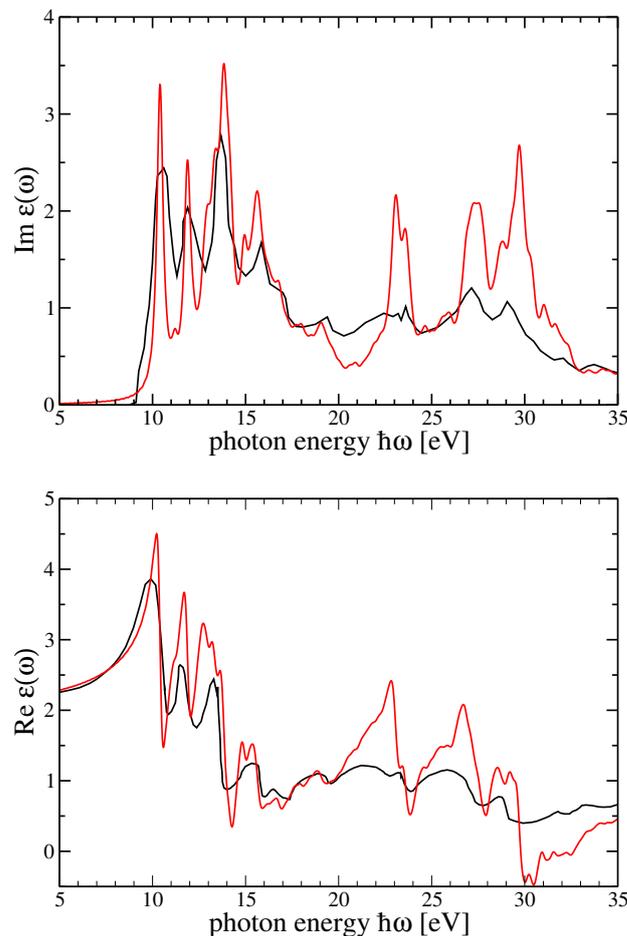

Figure 6. Dielectric function of c-SrF_2 calculated in the BSE scheme on top of GW_0 energies (**top**: imaginary part, **bottom**: real part) in comparison with the experiment from Reference [29]. Red lines refer to our calculated spectra and black lines to the experimental data.

5. Summary and Conclusions

The electronic and optical properties of two alkaline earth metal fluorides, namely MgF_2 and SrF_2, which crystallize in structures of different symmetries, namely rutile, and fluorite, were calculated here. Ground-state energies, band structures, band-energy gaps,

and optical absorption spectra with the inclusion of quasiparticle and excitonic effects were produced using state-of-the-art computational schemes. Rutile MgF_2 distinguished the ground-state and excited-state properties with respect to the other cubic difluoride SrF_2. Cubic SrF_2 properties are similar to those of the other remaining bulk systems of the family of alkaline earth metal, namely cubic CaF_2 and BaF_2, as known from present and previous calculations. The QP corrections with respect to HSE06 band gaps and the excitonic binding energies are consistent, and respectively of the order of 3.8 eV and 1.1 eV for rutile MgF_2, and 3.3 eV and 1.6 eV for cubic SrF_2. For rutile MgF_2, we give—for the first time—highly-converged results on optical, excitation, and screening properties for the two principal directions of the crystal. A comparison was also given between the present data for the bulk and the recently published excitation and optical properties relative to the corresponding fluoride clusters, confirming strong excitonic effects occurring in the finite-sized SrF_2/MgF_2 systems. The present results could be useful regarding possible photolithography MgF_2/SrF_2 applications and with respect to the renewed interest in UV disinfection materials.

6. Additional Material: Bulk Systems versus Clusters

Recent studies on the electronic and optical properties and alkaline earth metal fluoride clusters have emerged in recent years [38–42]. These studies were motivated by basic research interests and possible applications.

In Reference [38], some of the authors of the present collaboration focused on the $(MF_2)_n$ systems with $n = 1, 2, 3$ and M=Mg,Ca,Sr,Ba, i.e., their attention was focused on fluoride clusters, for the (first) smallest three members of each family. The results for bulk crystals r-MgF_2 and c-SrF_2 proposed in the present paper allow completing the systematic comparison for excited state and optical properties determined within state-of-the-art techniques with those of the corresponding clusters. The comparison may play an important role in understanding the effects of nanostructuring in the electronic and optical properties of the fluorides under study. In Table 6, the quasiparticle gap (E_{gap}), the optical onset (E_{opt}), and the binding energy of the exciton (E_{Bind}) are reported for the bulk systems and the corresponding clusters. The evaluation of these observables in the case of the clusters was performed using well-tested techniques specific to these systems [38,87]. In Table 6, the ranges of each physical observable relative to the smallest three clusters for MgF_2 and SrF_2 were reported. For more details, see Reference [38].

Table 6. Excited and optical properties of the clusters $(MgF_2)_n$ and $(SrF_2)_n$, $n = 1, 2, 3$ and the crystalline solids (r-MgF_2 and c-SrF_2). The quasiparticle gap E_{gap}, the optical onset E_{opt}, and the binding energy of the exciton E_b are displayed. In the first row, we report the data on the $(MgF_2)_n$ clusters, in the second, we present the data on the solid r-MgF_2 from Reference [37], in the third, we present the outcomes of the present work for solid r-MgF_2 with experimental data in parentheses. In the last two rows, the data for $(SrF_2)_n$ clusters and solid c-SrF_2 are given. The outcomes for the clusters are from Reference [38].

	E_{gap} [eV]	E_{Peak} [eV]	E_{Bind} [eV]
Clusters $(MgF_2)_n$	11.45–12.49	6.56–6.78	4.49–5.71
Solid r-MgF_2 (Present)	13.24 (12.4)	11.8 (11.6)	1.4 (0.8)
Solid r-MgF_2 (Other)	12.17	10.90	1.13
Clusters $(SrF_2)_n$	9.33–10.16	5.10–5.26	4.23–4.9
Solid c-SrF_2 (Present)	11.82 (11.25)	10.4 (10.6)	1.4(0.65)

In the first row, we list the data for the $(MgF_2)_n$ clusters, in the second, we list the data for solid r-MgF_2 from Reference [37], and in the third row, we list the outcomes of the

present work for solid r-MgF$_2$ with experimental data in parentheses. In the last two rows, the data for (SrF$_2$)$_n$ clusters and solid c-SrF$_2$ are listed. As far as the excitation properties are concerned, the quasiparticle band-gap energies of the clusters are similar to those of the bulk systems. On the other hand, the comparison of the energies of the optical onset shows large changes from the bulk to clusters.

The onset energy of r-MgF$_2$ jumps from 10.9 eV, an energy located in the extreme UV (EUV: 10–124 eV) for bulk to an average value of 6.7 eV, and energy belonging to the far UV (FUV: 4.13–10.16 eV) for the clusters. In the case of bulk c-SrF$_2$, the onset energy is 10.4 eV (high border of FUV) and the average value for the corresponding clusters is 5.18 eV, with an energy in the middle UV range (MUV: 3.10–4.13 eV). Therefore, the onset energies of the clusters take place in different UV domains with respect to their corresponding bulk systems. This happens because specific molecular transitions take place for the clusters at energies for which the bulk system does not display the allowed electronic transitions.

The large differences in E$_{opt}$ between clusters and bulk have important consequences on the exciton binding energies, which results in strongly enhanced clusters. The interplay between the confinement effects and reduced screening can be considered the main reason for that. Here, it is confirmed that MgF$_2$ and SrF$_2$, if prepared as (small) clusters or as bulk samples, show very different UV properties (e.g., absorption). This can have very different application-related consequences for the design of UV-operating devices.

Author Contributions: Conceptualization, G.C. and F.B.; Software, J.F.; Validation, G.C. and F.B.; Formal analysis, F.B. and S.B.; Investigation, G.C., J.F. and S.B.; Resources, G.C.; Data curation, G.C., J.F. and S.B.; Writing—original draft, G.C.; Writing—review & editing, J.F., F.B. and S.B.; Visualization, J.F.; Supervision, G.C. and S.B.; Funding acquisition, G.C. All authors have read and agreed to the published version of the manuscript.

References

1. Rubloff, G.W. Far-Ultraviolet Reflectance Spectra and the Electronic Structure of Ionic Crystals. *Phys. Rev. B* **1972**, *5*, 662–684. [CrossRef]
2. Zemann, J. Crystal structures, 2nd edition. Vol. 1, by R. W. G. Wyckoff. *Acta Crystallogr.* **1965**, *18*, 139. [CrossRef]
3. Bechstedt, F. *Many-Body Approach to Electronic Excitations*; Springer: Berlin/Heidelberg, Germany, 2015. [CrossRef]
4. Bordonaro, G.J. DUV Photolithography and Materials. In *Encyclopedia of Nanotechnology*; Bhushan, B., Ed.; Springer: Dordrecht, The Netherlands, 2012; pp. 590–604. [CrossRef]
5. Bertoni, C.M.; Cappellini, G.; Finocchi, F.; Monachesi, P. 7.3.4 CaF$_2$ and other fluorides surfaces. In *Physics of Solid Surfaces*; Springer: Berlin/Heidelberg, Germany, 2015; pp. 387–391. [CrossRef]
6. Mattila, T.; Pöykkö, S.; Nieminen, R.M. Ab initio study of point defects in CdF$_2$. *Phys. Rev. B* **1997**, *56*, 15665–15671. [CrossRef]
7. Shi, H.; Eglitis, R.I.; Borstel, G. Ab initio calculations of the BaF$_2$ bulk and surface F centers. *J. Phys. Condens. Matter* **2006**, *18*, 8367–8381. [CrossRef]
8. Jia, R.; Shi, H.; Borstel, G. The atomic and electronic structure of CaF$_2$ and BaF$_2$ crystals with H centers: A hybrid DFT calculation study. *J. Phys. Condens. Matter* **2010**, *22*, 055501 . [CrossRef]
9. Tousey, R. Optical Constants of Fluorite in the Extreme Ultraviolet. *Phys. Rev.* **1936**, *50*, 1057–1066. [CrossRef]
10. Samara, G.A. Temperature and pressure dependences of the dielectric properties of PbF2and the alkaline-earth fluorides. *Phys. Rev. B* **1976**, *13*, 4529–4544. [CrossRef]
11. Scrocco, M. Satellites in X-ray photoelectron spectroscopy of insulators. I. Multielectron excitations in CaF$_2$, SrF$_2$, and BaF$_2$. *Phys. Rev. B* **1985**, *32*, 1301–1305. [CrossRef]
12. Weesner, F.J.; Wright, J.C.; Fontanella, J.J. Laser spectroscopy of ion-size effects on point-defect equilibria in PbF$_2$:Eu^{3+}. *Phys. Rev. B* **1986**, *33*, 1372–1380. [CrossRef]

13. Kosacki, I.; Langer, J.M. Fundamental absorption edge of PbF2 and $Cd_{1-x}Pbx F_2$ crystals. *Phys. Rev. B* **1986**, *33*, 5972–5973. [CrossRef]

14. Hull, S.; Keen, D.A. Effect of hydrostatic pressure on the crystal structure and superionic behavior of lead (II) fluoride. *Phys. Rev. B* **1998**, *58*, 14837–14844. [CrossRef]

15. Fujita, M.; Itoh, M.; Bokumoto, Y.; Nakagawa, H.; Alov, D.L.; Kitaura, M. Optical spectra and electronic structures of lead halides. *Phys. Rev. B* **2000**, *61*, 15731–15737. [CrossRef]

16. Burnett, J.; Levine, Z.; Shirley, E. Intrinsic birefringence in calcium fluoride and barium fluoride. *Phys. Rev. B* **2001**, *64*, 241102–1–241102–4. [CrossRef]

17. Inagaki, H.; Saito, A.; Sugiyama, H.; Okabayashi, T.; Fujimoto, S. Rapid inactivation of SARS-CoV-2 with deep-UV LED irradiation. *Emerg. Microbes Infect.* **2020**, *9*, 1744–1747. [CrossRef]

18. Hessling, M.; Hoenes, K.; Vatter, P.; Lingenfelder, C. Ultraviolet irradiation doses for coronavirus inactivation - review and analysis of coronavirus photoinactivation studies. *GMS Hyg. Infect. Control.* **2020**, *15*, Doc08. [CrossRef] [PubMed]

19. Kowalski, W. UVGI Disinfection Theory. In *Ultraviolet Germicidal Irradiation Handbook*; Springer: Berlin/Heidelberg, Germany, 2009; pp. 17–50. [CrossRef]

20. Budowsky, E.I.; Bresler, S.E.; Friedman, E.A.; Zheleznova, N.V. Principles of selective inactivation of viral genome. *Arch. Virol.* **1981**, *68*, 239–247. [CrossRef]

21. Molteni, E.; Fratesi, G.; Cappellini, G.; Onida, G. Optical Properties of Free and Si(001)-Adsorbed Pyrimidinic Nucleobases. *Phys. Status Solidi (b)* **2017**, *255*, 1700497. [CrossRef]

22. Molteni, E.; Cappellini, G.; Onida, G.; Fratesi, G. Optical properties of organically functionalized silicon surfaces: Uracil-like nucleobases on Si(001). *Phys. Rev. B* **2017**, *95*, 05437–1–05437–8. [CrossRef]

23. Cadelano, E.; Cappellini, G. Electronic structure of fluorides: General trends for ground and excited state properties. *Eur. Phys. J. B* **2011**, *81*, 115–120. [CrossRef]

24. Cadelano, E.; Furthmüller, J.; Cappellini, G.; Bechstedt, F. One- and two-particle effects in the electronic and optical spectra of barium fluoride. *J. Phys. Condens. Matter* **2014**, *26*, 125501. [CrossRef]

25. Cappellini, G.; Furthmüller, J.; Cadelano, E.; Bechstedt, F. Electronic and optical properties of cadmium fluoride: The role of many-body effects. *Phys. Rev. B* **2013**, *87*, 075203–1–075203–9. [CrossRef]

26. Filippetti, A.; Fiorentini, V. A practical first-principles band-theory approach to the study of correlated materials. *Eur. Phys. J. B* **2009**, *71*, 139–183. [CrossRef]

27. Ferreira, L.G.; Pelá, R.R.; Teles, L.K.; Marques, M.; Jr., M.R.; Furthmülller, J. The LDA-1/2 technique: Recent Developments. In Proceedings of the 31st International Conference on the Physics of Semiconductors (ICPS), Zurich, Switzerland, 29 July–3 August 2012; AIP: Long Island, NY, USA, 2013; Volume 1566, pp. 27–28. [CrossRef]

28. Matusalem, F.; Marques, M.; Teles, L.K.; Filippetti, A.; Cappellini, G. Electronic properties of fluorides by approximated quasiparticle DFT-1/2 and PSIC methods: BaF_2, CaF_2 and CdF_2 as test cases. *J. Phys. Condens. Matter* **2018**, *30*, 365501. [CrossRef] [PubMed]

29. Frandon, J.; Lahaye, B.; Pradal, F. Spectra of Electronic Excitations in CaF_2, SrF_2, and BaF_2 in the 8 to 150 eV Range. *Phys. Status Solidi (b)* **1972**, *53*, 565–575. [CrossRef]

30. Raisin, C.; Berger, J.M.; Robin-Kandare, S. UPS and XPS spectra of CdF_2 and SrF_2 and interpretation of optical properties of these compounds. *J. Phys. C Solid State Phys.* **1980**, *13*, 1835–1844. [CrossRef]

31. Kudrnovský, J.; Christensen, N.E.; Maek, J. Electronic structure of fluorite-type compounds and mixed crystals. *Phys. Rev. B* **1991**, *43*, 12597–12606. [CrossRef]

32. Khenata, R.; Daoudi, B.; Sahnoun, M.; Baltache, H.; Rérat, M.; Reshak, A.H.; Bouhafs, B.; Abid, H.; Driz, M. Structural, electronic and optical properties of fluorite-type compounds. *Eur. Phys. J. B* **2005**, *47*, 63–70. [CrossRef]

33. Ivanovskikh, K.; Pustovarov, V.; Shulgin, B. Time-resolved luminescent VUV-spectroscopy of pure and doped by rare earth ions crystals of strontium fluoride. *Nucl. Instruments Methods Phys. Res. Sect. A Accel. Spectrometers, Detect. Assoc. Equip.* **2005**, *543*, 229–233. [CrossRef]

34. Jaiswal, S.R.; Sawala, N.S.; Nagpure, P.A.; Barde, W.S.; Omanwar, S. The Highly Efficient Inorganic SrF_2:Gd^{3+},Eu^{3+} Phosphor for Mercury Free Fluorescence Lamps. *Adv. Mater. Res.* **2022**, *1171*, 17–24. [CrossRef]

35. Chaney, R.C. Self-consistent energy band structure of magnesium fluoride using the LCAO method. *J. Phys. C Solid State Phys.* **1980**, *13*, 5691–5699. [CrossRef]

36. Vassilyeva, A.; Eglitis, R.; Kotomin, E.; Dauletbekova, A. Ab initio calculations of the atomic and electronic structure of MgF2 (011) and (111) surfaces. *Open Phys.* **2011**, *9*, 515–518. [CrossRef]

37. Yi, Z.; Jia, R. Quasiparticle band structures and optical properties of magnesium fluoride. *J. Phys. Condens. Matter* **2012**, *24*, 085602(5pp). [CrossRef] [PubMed]

38. Cappellini, G.; Bosin, A.; Serra, G.; Furthmüller, J.; Bechstedt, F.; Botti, S. Electronic and Optical Properties of Small Metal Fluoride Clusters. *ACS Omega* **2020**, *5*, 13268–13277. [CrossRef] [PubMed]

39. Levy, J.B.; Hargittai, M. Unusual Dimer Structures of the Heavier Alkaline Earth Dihalides: A Density Functional Study. *J. Phys. Chem. A* **2000**, *104*, 1950–1958. [CrossRef]

40. Koput, J.; Roszczak, A. CaF_2 As a Quasilinear Molecule: The Vibrational-Rotational Energy Levels Predicted by Ab Initio Quantum Chemistry Approach. *J. Phys. Chem. A* **2004**, *108*, 9267–9273. [CrossRef]

41. Pandey, R.K.; Waters, K.; Nigam, S.; He, H.; Pingale, S.S.; Pandey, A.C.; Pandey, R. A theoretical study of structural and electronic properties of alkaline-earth fluoride clusters. *Comput. Theor. Chem.* **2014**, *1043*, 24–30. [CrossRef]

42. Calder, V.; Mann, D.E.; Seshadri, K.S.; Allavena, M.; White, D. Geometry and Vibrational Spectra of Alkaline-Earth Dihalides. II. CaF_2, SrF_2, and BaF_2. *J. Chem. Phys.* **1969**, *51*, 2093–2099. [CrossRef]

43. Kresse, G.; Furthmüller, J. Efficiency of ab-initio total energy calculations for metals and semiconductors using a plane-wave basis set. *Comput. Mater. Sci.* **1996**, *6*, 15–50. [CrossRef]

44. Kresse, G.; Furthmüller, J. Efficient iterative schemes for ab initio total-energy calculations using a plane-wave basis set. *Phys. Rev. B* **1996**, *54*, 11169–11186. [CrossRef]

45. Vinet, P.; Rose, J.H.; Ferrante, J.; Smith, J.R. Universal features of the equation of state of solids. *J. Phys. Condens. Matter* **1989**, *1*, 1941–1963. [CrossRef]

46. Perdew, J.P.; Ruzsinszky, A.; Csonka, G.I.; Vydrov, O.A.; Scuseria, G.E.; Constantin, L.A.; Zhou, X.; Burke, K. Restoring the Density-Gradient Expansion for Exchange in Solids and Surfaces. *Phys. Rev. Lett.* **2008**, *100*, 136406–1–136406–4. [CrossRef]

47. Aroyo, M.I. (Ed.) *Teaching Edition of International Tables for Crystallography: Crystallographic Symmetry*; IUCr/Wilet: Chester, UK, 2021; ISBN 978-0-470-97422-3

48. Perdew, J.P.; Burke, K.; Ernzerhof, M. Generalized Gradient Approximation Made Simple. *Phys. Rev. Lett.* **1996**, *77*, 3865–3868. [CrossRef]

49. Armiento, R.; Mattsson, A.E. Functional designed to include surface effects in self-consistent density functional theory. *Phys. Rev. B* **2005**, *72*, 085108–1–085108–5. [CrossRef]

50. Perdew, J.P.; Zunger, A. Self-interaction correction to density-functional approximations for many-electron systems. *Phys. Rev. B* **1981**, *23*, 5048–5079. [CrossRef]

51. Haines, J.; Léger, J.M.; Gorelli, F.; Klug, D.D.; Tse, J.S.; Li, Z.Q. X-ray diffraction and theoretical studies of the high-pressure structures and phase transitions in magnesium fluoride. *Phys. Rev. B* **2001**, *64*, 134110–1–134110–10. [CrossRef]

52. Subhadra, K.; Hussain, K.A.; Hussain, W.; Sirdeshmukh, D.B. Thermal expansion of strontium fluoride. *J. Mater. Sci. Lett.* **1985**, *4*, 777–778. [CrossRef]

53. Gerlich, D. Elastic Constants of Strontium Fluoride between 4.2 and 300 °K. *Phys. Rev.* **1964**, *136*, A1366–A1368. [CrossRef]

54. Hedin, L. New Method for Calculating the One-Particle Green's Function with Application to the Electron-Gas Problem. *Phys. Rev.* **1965**, *139*, A796–A823. [CrossRef]

55. Godby, R.W.; Schlüter, M.; Sham, L.J. Self-energy operators and exchange-correlation potentials in semiconductors. *Phys. Rev. B* **1988**, *37*, 10159–10175. [CrossRef]

56. Bechstedt, F.; Sole, R.D.; Cappellini, G.; Reining, L. An efficient method for calculating quasiparticle energies in semiconductors. *Solid State Commun.* **1992**, *84*, 765–770. [CrossRef]

57. Onida, G.; Reining, L.; Rubio, A. Electronic excitations: Density-functional versus many-body Green's-function approaches. *Rev. Mod. Phys.* **2002**, *74*, 601–659. [CrossRef]

58. Sangalli, D.; Ferretti, A.; Miranda, H.; Attaccalite, C.; Marri, I.; Cannuccia, E.; Melo, P.; Marsili, M.; Paleari, F.; Marrazzo, A.; et al. Many-body perturbation theory calculations using the yambo code. *J. Phys. Condens. Matter* **2019**, *31*, 325902. [CrossRef]

59. Seidl, A.; Görling, A.; Vogl, P.; Majewski, J.A.; Levy, M. Generalized Kohn-Sham schemes and the band-gap problem. *Phys. Rev. B* **1996**, *53*, 3764–3774. [CrossRef]

60. Bechstedt, F.; Fuchs, F.; Kresse, G. Ab-initio theory of semiconductor band structures: New developments and progress. *Phys. Status Solidi (b)* **2009**, *246*, 1877–1892. [CrossRef]

61. Borlido, P.; Aull, T.; Huran, A.W.; Tran, F.; Marques, M.A.L.; Botti, S. Large-Scale Benchmark of Exchange–Correlation Functionals for the Determination of Electronic Band Gaps of Solids. *J. Chem. Theory Comput.* **2019**, *15*, 5069–5079. [CrossRef] [PubMed]

62. Heyd, J.; Scuseria, G.E.; Ernzerhof, M. Hybrid functionals based on a screened Coulomb potential. *J. Chem. Phys.* **2003**, *118*, 8207–8215. [CrossRef]

63. Krukau, A.V.; Vydrov, O.A.; Izmaylov, A.F.; Scuseria, G.E. Influence of the exchange screening parameter on the performance of screened hybrid functionals. *J. Chem. Phys.* **2006**, *125*, 224106–1–224106–5. [CrossRef] [PubMed]

64. Stankovski, M.; Antonius, G.; Waroquiers, D.; Miglio, A.; Dixit, H.; Sankaran, K.; Giantomassi, M.; Gonze, X.; Côté, M.; Rignanese, G.M. G0W0 band gap of ZnO: Effects of plasmon-pole models. *Phys. Rev. B* **2011**, *84*, 241201–1–241201–5. [CrossRef]

65. Cappellini, G.; Sole, R.D.; Reining, L.; Bechstedt, F. Model dielectric function for semiconductors. *Phys. Rev. B* **1993**, *47*, 9892–9895. [CrossRef]

66. Schmidt, W.G.; Glutsch, S.; Hahn, P.H.; Bechstedt, F. Efficient (N^2) method to solve the Bethe-Salpeter equation. *Phys. Rev. B* **2003**, *67*, 085307–1–085307–7. [CrossRef]

67. Caruso, F.; Rinke, P.; Ren, X.; Scheffler, M.; Rubio, A. Unified description of ground and excited states of finite systems: The self-consistentGWapproach. *Phys. Rev. B* **2012**, *86*, 081102–1–081102–5. [CrossRef]

68. Vassilyeva, A.; Eglitis, R.; Kotomin, E.; Dauletbekova, A. *Ab initio* calculations of MgF_2 (001) and (011) surface structure. *Phys. B Cond. Matt.* **2010**, *405*, 2125–2127. [CrossRef]

69. Jia, R.; Shi, H.; Borstel, G. Ab initio calculations for SrF_2 with F- and M-centers. *Comp. Mat. Sci.* **2008**, *43*, 980–988. [CrossRef]

70. Yue, L.; Jia, R.; Shi, H.; He, X.; Eglitis, R.I. First-Principles Calculations for the H Center in SrF_2 Crystals. *J. Phys. Chem. A* **2010**, *114*, 8444–8449. [CrossRef]

71. Jibran, M.; Murtaza, G.; Khan, M.; Khenata, R.; Muhmmad, S.; Ali, R. First principle study of MF2 (M=Mg, Ca, Sr, Ba, Ra) compounds. *Comp. Mater. Sci.* **2014**, *81*, 575–581. [CrossRef]

72. Kolobanov, V.N.; Mikhailin, V.V.; Chernov, S.P.; Spassky, D.A.; Makhov, V.N.; Kirm, M.; Feldbach, E.; Vielhauer, S. Luminescence of singlet self-trapped excitons in MgF_2. *J. Phys. Condens. Matter* **2009**, *21*, 375501. [CrossRef] [PubMed]

73. Lisitsyn, V.; Lisitsyna, L.; Popov, A.; Kotomin, E.; Abuova, F.; Akilbekov, A.; Maier, J. Stabilization of primary mobile radiation defects in MgF_2 crystals. *Nucl. Instruments Methods Phys. Res. Sect. B Beam Interact. Mater. Atoms* **2016**, *374*, 24–28. [CrossRef]

74. Shishkin, M.; Kresse, G. Self-consistent GW calculations for semiconductors and insulators. *Phys. Rev. B* **2007**, *75*. [CrossRef]

75. Golze, D.; Keller, L.; Rinke, P. Accurate Absolute and Relative Core-Level Binding Energies from *GW*. *J. Phys. Chem. Lett.* **2020**, *11*, 1840–1847. [CrossRef]

76. Li, J.; Jin, Y.; Rinke, P.; Yang, W.; Golze, D. Benchmark of *GW* Methods for Core-Level Binding Energies. *J. Chem. Theory Comput.* **2022**, *18*, 7570–7585. [CrossRef]

77. Li, J.; Golze, D.; Yang, W. Combining Renormalized Singles *GW* Methods with the Bethe–Salpeter Equation for Accurate Neutral Excitation Energies. *J. Chem. Theory Comput.* **2022**, *18*, 6637–6645. [CrossRef]

78. Eglitis, R.I.; Purans, J.; Jia, R. Comparative Hybrid Hartree-Fock-DFT Calculations of WO_2-Terminated Cubic WO_3 as Well as $SrTiO_3$, $BaTiO_3$, $PbTiO_3$ and $CaTiO_3$ (001) Surfaces. *Crystals* **2021**, *11*, 455. [CrossRef]

79. Botti, S.; Marques, M.A.L. Strong Renormalization of the Electronic Band Gap due to Lattice Polarization in the GW Formalism. *Phys. Rev. Lett.* **2013**, *110*. [CrossRef] [PubMed]

80. Lambrecht, W.R.L.; Bhandari, C.; van Schilfgaarde, M. Lattice polarization effects on the screened Coulomb interaction W of the GW approximation. *Phys. Rev. Mater.* **2017**, *1*. [CrossRef]

81. Cao, H.; Yu, Z.; Lu, P.; Wang, L.W. Fully converged plane-wave-based self-consistent GW calculations of periodic solids. *Phys. Rev. B* **2017**, *95*. [CrossRef]

82. Albert, J.P.; Jouanin, C.; Gout, C. Electronic energy bands in the fluorite structure: CaF_2 and CdF_2. *Phys. Rev. B* **1977**, *16*, 4619–4629. [CrossRef]

83. Fox, M. *Optical Properties of Solids*; Oxford University Press: Oxford, UK, 2001; Volume 384, p. 416.

84. Wannier, G.H. The Structure of Electronic Excitation Levels in Insulating Crystals. *Phys. Rev.* **1937**, *52*, 191–197. [CrossRef]

85. Satta, G.; Cappellini, G.; Olevano, V.; Reining, L. Many-body effects in the electronic spectra of cubic boron nitride. *Phys. Rev. B* **2004**, *70*, 195212–1–195212–13. [CrossRef]

86. Kammerlander, D.; Botti, S.; Marques, M.A.L.; Marini, A.; Attaccalite, C. Speeding up the solution of the Bethe-Salpeter equation by a double-grid method and Wannier Wannier interpolation. *Phys. Rev. B* **2012**, *86*, 125203–1–125203–5. [CrossRef]

87. Mocci, P.; Malloci, G.; Bosin, A.; Cappellini, G. Time-Dependent Density Functional Theory Investigation on the Electronic and Optical Properties of Poly-C,Si,Ge-acenes. *ACS Omega* **2020**, *5*, 16654–16663. [CrossRef]